

# Search for Antihelium in Cosmic Rays

The AMS Collaboration

## Abstract

The Alpha Magnetic Spectrometer (AMS) was flown on the space shuttle *Discovery* during flight STS–91 in a  $51.7^\circ$  orbit at altitudes between 320 and 390 km. A total of  $2.86 \times 10^6$  helium nuclei were observed in the rigidity range 1 to 140 GV. No antihelium nuclei were detected at any rigidity. An upper limit on the flux ratio of antihelium to helium of  $< 1.1 \times 10^{-6}$  is obtained.

Submitted to *Phys. Lett. B*

# Introduction

The existence (or absence) of antimatter nuclei in space is closely connected with the foundation of the theories of elementary particle physics, CP-violation, baryon number nonconservation, Grand Unified Theory (GUT), etc. Balloon-based cosmic ray searches for antinuclei at altitudes up to 40 km have been carried out for more than 20 years; all such searches have been negative [1–7]. The absence of annihilation gamma ray peaks excludes the presence of large quantities of antimatter within a distance of the order of 10 Mpc from the earth. The baryogenesis models are not yet supported by particle physics experimental data. To date baryon nonconservation and large levels of CP-violation have not been observed. The Alpha Magnetic Spectrometer (AMS) [8] is scheduled for a high energy physics program on the International Space Station. In addition to searching for dark matter and the origin of cosmic rays, a major objective of this program is to search for antinuclei using an accurate, large acceptance magnetic spectrometer. AMS was flown on the space shuttle *Discovery* on flight STS-91 in June 1998. This was primarily a test flight that would enable the AMS team to gather data on background sources, adjust operating parameters and verify the detector's performance under actual space flight conditions. A search for antihelium nuclei using the data collected during this precursor flight is reported. The signal investigated is nuclei with charge  $Z = -2$ .

## AMS on STS-91

A schematic cross section in the bending plane of AMS as flown on STS-91, Fig. 1, shows the permanent magnet, tracker, time of flight hodoscopes, Cerenkov counter and anticoincidence counters. The AMS coordinate system, as shown, coincides with the shuttle coordinate system, with the z-axis (up in the figure) pointing out of the shuttle payload bay and the x-axis pointing towards the tail of the shuttle. The geometric acceptance was  $\sim 0.3 \text{ m}^2\text{sr}$ . AMS as flown on STS-91 will be described in detail elsewhere [9].

The magnet provided the analyzing power of the spectrometer. It was made of 1.9 tons of Nd-Fe-B in the shape of a cylindrical shell of inner diameter 1115 mm and length 800 mm. The Nd-Fe-B was magnetized to 46 MGoe with the direction varying to provide a dipole field in the x direction, perpendicular to the cylinder axis. At the center the magnetic field was 0.14 Tesla and the analyzing power,  $BL^2$ , was 0.14 Tm<sup>2</sup>.

The trajectory of charged particles traversing the magnet bore was observed with a tracker made of six planes, T1 to T6, of double sided silicon microstrip detectors [10]. For AMS on STS-91 half of the tracker area was equipped. From the deflection the rigidity,  $R = pc/|Z|e$  (GV), was measured. The tracker also provided a determination of charge magnitude,  $|Z|$ , through multiple energy loss measurements. Special care was taken to minimize the amount of material in the tracker construction; the total amount of material within the tracker volume was less than 3% of a radiation length parallel to the z-axis. The tracker alignment was made first with metrology, continuously monitored with an infrared laser system and then verified with high momentum tracks from the CERN PS test beam. During flight hits in the tracker were measured with an accuracy of  $\sim 10 \mu\text{m}$  in the bending, or y, direction and  $\sim 30 \mu\text{m}$  in the x and z directions. The resolution in terms of rigidity was verified for  $|Z| \geq 2$  nuclei using helium and carbon ion beams at GSI-Darmstadt. Fig. 2 shows the rigidity resolution for  $Z = 2$  flight data and the agreement with the  $Z = 2$  helium data measured at GSI. Note that at low momenta the resolution was limited by multiple scattering.

The particle direction and velocity were measured with a four layer, S1 to S4, time-of-flight (TOF) hodoscope. Each layer consisted of 14 scintillator paddles of thickness 10 mm, width 110 mm, hermetically arranged with a 5 mm overlap. As shown in Fig. 1, two layers were above the magnet

and two below. The paddles in each pair were orthogonal. The pulse height information recorded from the TOF paddles provided an additional determination of  $|Z|$ . The typical accuracy of the time of flight measurements was 105 psec for  $|Z| = 2$ . Fig. 3 shows the velocity,  $\beta = v/c$ , resolution for high rigidity  $|Z| = 2$  particles.

The velocity measurement was complemented by a threshold Cerenkov counter made of aerogel with a refractive index of 1.035.

A layer of anticoincidence scintillation counters (ACC) covered the inner surface of the magnet to reject the background caused by particles passing through or interacting in the magnet walls and support structures. The detector was also shielded from low energy (up to several MeV) particles by thin carbon fiber walls (LEPS). For particles arriving from above, as shown in Fig. 1, the amount of material at normal incidence was  $1.5 \text{ g/cm}^2$  in front of the TOF system, and  $3.5 \text{ g/cm}^2$  in front of the tracker.

During construction, the detector components went through extensive space qualification tests (acceleration, vibration, thermal vacuum, electromagnetic interference and radiation). For example, the magnet was tested in a centrifuge to 17.7 g. Key electronics components were tested at Dubna in heavy ion beams of Ne, Ar and Kr.

During flight the detector was located in the payload bay of the space shuttle and operated in vacuum. Events were triggered by the coincidence of signals in all four TOF planes consistent with the passage of a charged particle through the active tracker volume. Triggers with a coincident signal from the ACC were vetoed. The detector performance as well as temperature and magnetic field were monitored continuously. A total of 100 million triggers were recorded.

After the flight, the detector was checked again:

- first, the detector was placed in a heavy ion (He, C) beam from 1.0 to 5.6 GV at 600 different incident angles. This test was done with a total of 45 million events and was carried out at GSI–Darmstadt.
- second, the detector was placed in a proton and pion beam at CERN with momentum from 2 to 14 GeV at 1200 different incident angles. This test was done with a total of 100 million events.

The continued monitoring of the detector confirmed that the detector performance before, during and after the flight remained the same. In particular, the alignment of the silicon tracker remained the same to an accuracy of  $\sim 5 \mu\text{m}$ .

## Event Selection

After the shuttle had attained orbit, data collection commenced on 3 June 1998 and continued over the next nine days for a total of 184 hours. During data taking the shuttle altitude varied from 320 to 390 km and the latitude ranged between  $\pm 51.7$  degrees. Before rendezvous with the MIR space station the attitude of the shuttle was maintained to keep the z-axis of AMS (see Fig. 1) pointed within 45 degrees of the zenith. While docked, the attitude was constrained by MIR requirements and varied substantially. After undocking the pointing was maintained within 1, 20 and then 40 degrees of the zenith. Shortly before descent the shuttle turned over and the pointing was towards the nadir. For this search, data collected while passing through the South Atlantic Anomaly was excluded.

The procedure to search for antihelium began with event reconstruction, which included:

- Measurement of the particle rigidity,  $R$ , from the deflection of the trajectory measured by the tracker in the magnetic field. To ensure that the particle was well measured, hits in at least four tracker planes were required and the fitting was performed with two different algorithms, the results of which were required to agree.
- Measurement of the particle velocity,  $\beta$ , and direction,  $\hat{z} = \pm 1$ , from the TOF, where  $\hat{z} = -1$  signifies a downward going particle in Fig. 1.
- Determination of the magnitude of the particle charge,  $|Z|$ , from the measurements of energy losses in the TOF counters and tracker planes (corrected for  $\beta$ ).

From this reconstruction the sign of the particle charge was derived from the deflection in the rigidity fit and the direction. The particle mass was derived from  $|Z|R$  and  $\beta$ .

The major backgrounds to the antihelium ( $Z = -2$ ) search are the abundant amount of protons and electrons ( $|Z| = 1$ ) and helium ( $Z = +2$ ). To distinguish antihelium from  $e^-$ ,  $p$  and  $He$ , the detector response to  $e^-$ ,  $p$  and  $He$  was studied in three ways:

- (i) from the  $e^-$ ,  $p$  and  $He$  data collected in flight.
- (ii) from the  $He$  beam data at GSI and the  $p$  beam data at the CERN PS.
- (iii) from Monte Carlo studies of (i) and (ii).

Key points in the selection for  $\bar{He}$  events and the rejection of background were:

**to select events with  $|Z| = 2$ :** This was to ensure no contamination from  $|Z| = 1$  events with a wrongly measured charge magnitude which would mimic  $|Z| > 1$  events. Fig. 4 shows the energy deposition and the assigned charge magnitude as measured independently by the TOF and the tracker. The probability of the wrong charge magnitude being assigned by the combined TOF and tracker measurements was estimated to be less than  $10^{-7}$ .

**to determine the sign of  $|Z| = 2$  events:** This was to distinguish  $He$  from  $\bar{He}$ . This was done with the following method:

- (i) **Identify the particle direction:** measurement of the particle direction leads to the correct assignment of the sign of the charge. Fig. 5 shows the particle direction,  $\hat{z}/\beta$ , distribution. No events were observed between the  $\hat{z} = +1$  and  $\hat{z} = -1$  populations which indicates there was no leakage of particles from one population to the other and the direction was always correctly assigned.
- (ii) **Identify large angle nuclear scattering events:** events in which a single nuclear scattering in one of the inner tracker planes, T2–T5, introduced a large angle kink in the track and might cause an incorrect measurement of the charge sign. This background was suppressed by a cut on the estimated rigidity error. Additional suppression was achieved by requiring agreement for the rigidity and charge sign measured using all the hits in the tracker and separately in the first three hits and the last three hits along the track. Fig. 6 shows the asymmetry,  $A_{12} = (R_1 - R_2)/(R_1 + R_2)$ , of the rigidity measured with the first and last three hits along the track,  $R_1$  and  $R_2$ , and the cuts applied. From Fig. 6 we see that whereas these cuts reject much of the large angle scattering events (Fig. 6a), the cuts do not reject the genuine signal (Fig. 6b).

- (iii) **Identify events with collinear delta rays:** events with collinear debris, *e.g.* delta rays, from an interaction of the primary particle in the tracker material which may shift a measured point from the trajectory, leading to an incorrectly measured rigidity and charge sign. This background was efficiently rejected by an isolation cut which rejected events with an excess of energy observed within 5 mm of the track.

A probabilistic function was then constructed from measurements of the velocity, rigidity and energy loss which described the compatibility of these measurements with the passage of a helium or antihelium nucleus of mass  $A = 3$  or  $4$ . Fig. 7 shows the compatibility distribution for the antihelium candidates (Fig. 7a) and helium samples together with Monte Carlo predictions for the helium event distribution (Fig. 7b). As seen, the compatibility cut enables us to reject the small remaining background and keep nearly all of the helium sample.

The results of our search are summarized in Fig. 8. As seen, we obtain a total of  $2.86 \times 10^6$  He events up to a rigidity of 140 GV. We found no antihelium event at any rigidity.

## Results and Interpretation

Since no antihelium nuclei were observed, we can only establish an upper limit on their flux. Here three upper limits on this flux relative to the observed flux of helium nuclei are calculated which differ in the assumptions used for the antihelium rigidity spectrum. In the first it is assumed to have the same shape as the helium rigidity spectrum. In the second this spectrum is assumed to be uniform. Finally a conservative estimate is made independent of the antihelium rigidity spectrum.

All of these methods require the measured rigidity spectrum to be corrected for the detector resolution and efficiency as a function of the measured,  $R_m$ , and incident,  $R$ , rigidity. The detection efficiency including the rigidity resolution function,  $f(R, R_m)$ , was evaluated through complete Monte Carlo simulation using the GEANT Monte Carlo package [11]. The incident rigidity spectrum,  $dN'/dR$  was extracted from the measured spectrum,  $dN'/dR_m$ , by numerical deconvolution of  $dN'/dR_m = f(dN'/dR) \times f(R, R_m)dR$ . To obtain the detector efficiency for antihelium,  $\epsilon_{\bar{\text{He}}}(R)$ , a small correction was applied to the efficiency for helium nuclei,  $\epsilon_{\text{He}}(R)$ , based on the estimated [12] difference in absorption cross sections.

Letting  $N_{\text{He}}(R_i)$  be the number of incident helium nuclei in the rigidity bin  $(R_i, R_i + \Delta R)$  and  $N'_{\text{He}}(R_i)$  be the number of measured He in the same rigidity bin after correction for the detector resolution, then  $N'_{\text{He}}(R_i) = \epsilon_{\text{He}}(R_i)N_{\text{He}}(R_i)$ , where  $\epsilon_{\text{He}}(R_i)$  is the detection efficiency in this bin, and similarly for antihelium. Over the rigidity interval studied no  $\bar{\text{He}}$  were found,  $N'_{\bar{\text{He}}}(R_i) = 0$  for each  $i$ . At the 95 % confidence level this is taken to be less than 3 and the differential upper limit for the flux ratio is given by:

$$\frac{N_{\bar{\text{He}}}(R_i)}{N_{\text{He}}(R_i)} < \frac{3}{N'_{\text{He}}(R_i)/\epsilon_{\text{He}}(R_i)}. \quad (1)$$

The difference between  $\epsilon_{\bar{\text{He}}}(R_i)$  and  $\epsilon_{\text{He}}(R_i)$  is small, so these terms practically cancel and the results below are essentially independent of the detection efficiency.

- (i) If the incident  $\bar{\text{He}}$  spectrum is assumed to have the same shape as the He spectrum over the range  $1 < R < 140$  GV, then summing equation (1) yields a limit of:

$$\frac{N_{\bar{\text{He}}}}{N_{\text{He}}} < 1.1 \times 10^{-6}.$$

(ii) Assuming a uniform  $\bar{\text{He}}$  rigidity spectrum, and using a mean  $\bar{\text{He}}$  inverse detection efficiency,  $\langle 1/\varepsilon_{\bar{\text{He}}} \rangle = \sum(1/\varepsilon_{\bar{\text{He}}}(R_i))/n$ , and noting that  $N'_{\bar{\text{He}}} = \sum N'_{\bar{\text{He}}}(R_i) = 0$  which is also taken to be less than 3 at the 95 % C.L., summing equation (1) yields a limit of

$$\frac{N_{\bar{\text{He}}}}{N_{\text{He}}} = \frac{\sum N_{\bar{\text{He}}}(R_i)}{\sum N_{\text{He}}(R_i)} < \frac{3}{\sum N'_{\bar{\text{He}}}(R_i) / \varepsilon_{\bar{\text{He}}}(R_i)}, \quad (2)$$

which evaluates to  $\frac{N_{\bar{\text{He}}}}{N_{\text{He}}} < 1.8 \times 10^{-6}$  for  $R = 1.6$  to  $40$  GV

and  $\frac{N_{\bar{\text{He}}}}{N_{\text{He}}} < 3.9 \times 10^{-6}$  for  $R = 1.6$  to  $100$  GV.

(iii) For a conservative upper limit, which does not depend on the antihelium spectrum, equation (1) is summed from  $R_{min} = 1.6$  GV up to a variable  $R_{max}$  and instead of the mean value  $\langle 1/\varepsilon_{\bar{\text{He}}} \rangle$  the minimum value of this efficiency in the  $(R_{min}, R_{max})$  interval is taken, yielding

$$\frac{\sum N_{\bar{\text{He}}}(R_i)}{\sum N_{\text{He}}(R_i)} < \frac{3}{\sum N'_{\bar{\text{He}}}(R_i) / \varepsilon_{\bar{\text{He}}}^{\min}(R_{min}, R_{max})}, \text{ where } R_i = (R_{min}, R_{max}). \quad (3)$$

These results are shown in Fig. 9 as a function of  $R_{max}$ .

In conclusion, we found no antihelium nuclei at any rigidity. Up to rigidities of  $140$  GV,  $2.86 \times 10^6$  helium nuclei were measured. Assuming the antihelium rigidity spectrum to have the same shape as the helium spectrum, an upper limit at the 95 % confidence level on the relative flux of antihelium to helium of  $1.1 \times 10^{-6}$  was obtained. This result is an improvement in both sensitivity and rigidity range over previous measurements [7]. This flight has shown that the completed AMS on the International Space Station will provide many orders of magnitude of improvement in the sensitivity to search for antihelium.

## Acknowledgements

We thank Professors S. Ahlen, C. Canizares, A. De Rujula, J. Ellis, A. Guth, M. Jacob, L. Maiani, R. Mewaldt, R. Orava, J. F. Ormes and M. Salamon for helping us to initiate this experiment.

The success of the first AMS mission is due to many individuals and organizations outside of the collaboration. The support of NASA was vital in the inception, development and operation of the experiment. The dedication of Douglas P. Blanchard, Mark J. Sistilli, James R. Bates, Kenneth Bollweg and the NASA and Lockheed–Martin Mission Management team, the support of the Max–Plank Institute for Extraterrestrial Physics, the support of the space agencies from Germany (DLR), Italy (ASI), France (CNES) and China and the support of CSIST, Taiwan, made it possible to complete this experiment on time.

The support of CERN and GSI–Darmstadt, particularly of Professor Hans Specht and Dr. Reinhard Simon made it possible for us to calibrate the detector after the shuttle returned from orbit.

We are most grateful to the STS–91 astronauts, particularly to Dr. Franklin Chang–Diaz who provided vital help to AMS during the flight.

The support of INFN, Italy, ETH–Zürich, the University of Geneva, the Chinese Academy of Sciences, Academia Sinica and National Central University, Taiwan, the RWTH–Aachen, Germany, the University of Turku, the University of Technology of Helsinki, Finland, U.S. DOE and M.I.T. is gratefully acknowledged.

## References

- [1] G.F.Smoot *et al.*, Phys. Rev. Lett. **35** (1975) 258–261.
- [2] G.Steigman *et al.*, Ann. Rev. Astr. Ap. **14** (1976) 339.
- [3] G.Badhwar *et al.*, Nature **274** (1978) 137.
- [4] A.Buffington *et al.*, ApJ **248** (1981) 1179–1193.
- [5] R.L.Golden *et al.*, ApJ **479** (1997) 992.
- [6] J.F.Ormes *et al.*, ApJ Letters **482** (1997) L187.
- [7] T.Saeki *et al.*, Phys. Lett. **B422** (1998) 319.
- [8] S. Ahlen *et al.*, Nucl. Inst. Meth. **A350** (1994) 351.
- [9] AMS Collab, J. Alcaraz *et al.*, Nucl. Inst. Meth. , , in preperation;  
see also: G. M. Viertel, M. Capell, Nucl. Inst. Meth. **A 419** (1998) 295–299.
- [10] AMS Tracker Group, G. Ambrosi *et al.*, Nucl. Inst. Meth. (1999), to be submitted to NIM.
- [11] See R. Brun *et al.*, “GEANT 3”, CERN DD/EE/84-1 (Revised), September 1987.  
The FLUKA program (see P. A. Aamio, FLUKA Users Guide, CERN Report TIS-RP-190  
(1990)) is used to simulate hadronic interactions..
- [12] A.A.Moiseev and J.F.Ormes, Astroparticle Physics **6** (1997) 379–386.

## The AMS Collaboration:

J.Alcaraz<sup>x</sup> D.Alvisi<sup>i</sup> B.Alpat<sup>ab</sup> G.Ambrosi<sup>i</sup> H.Anderhub<sup>af</sup> L.Ao<sup>g</sup> A.Arefiev<sup>aa</sup> P.Azzarello<sup>i</sup> E.Babucci<sup>ab</sup> L.Baldini<sup>j,l</sup> M.Basile<sup>j</sup> D.Barancourt<sup>s</sup> F.Barao<sup>v,u</sup> G.Barbier<sup>s</sup> G.Barreira<sup>v</sup> R.Battiston<sup>ab</sup> R.Becker<sup>l</sup> U.Becker<sup>l</sup> L.Bellagamba<sup>l</sup> P.Béné<sup>r</sup> J.Berdugo<sup>x</sup> P.Berges<sup>l</sup> B.Bertucci<sup>ab</sup> A.Biland<sup>af</sup> S.Bizzaglia<sup>ab</sup> S.Blasko<sup>ab</sup> G.Boella<sup>v</sup> M.Bourquin<sup>r</sup> G.Bruni<sup>i</sup> M.Buenerd<sup>s</sup> J.D.Burger<sup>l</sup> W.J.Burger<sup>ab</sup> X.D.Cai<sup>l</sup> R.Cavalletti<sup>i</sup> C.Camps<sup>b</sup> P.Cannarsa<sup>af</sup> M.Capell<sup>l</sup> D.Casadei<sup>i</sup> J.Casaus<sup>s</sup> G.Castellini<sup>p</sup> Y.H.Chang<sup>w</sup> H.S.Chen<sup>i</sup> Z.G.Chen<sup>g</sup> N.A.Chernopolekov<sup>v</sup> A.Chiarini<sup>i</sup> T.H.Chiueh<sup>m</sup> Y.L.Chuang<sup>ac</sup> F.Cindolo<sup>l</sup> V.Commichau<sup>b</sup> A.Contin<sup>i</sup> A.Cotta-Ramusino<sup>l</sup> P.Crespo<sup>v</sup> M.Cristinziani<sup>i</sup> J.P.da Cunha<sup>n</sup> T.S.Dai<sup>l</sup> J.D.Deus<sup>u</sup> L.K.Ding<sup>i</sup> N.Dinu<sup>k</sup> L.Djambazov<sup>af</sup> I.D'Antone<sup>i</sup> Z.R.Dong<sup>h</sup> P.Emonet<sup>r</sup> F.J.Eppling<sup>l</sup> T.Eronen<sup>ae</sup> G.Esposito<sup>ab</sup> P.Extermann<sup>i</sup> J.Favier<sup>c</sup> C.C.Feng<sup>w</sup> E.Fiandrini<sup>ab</sup> F.Finelli<sup>l</sup> P.H.Fisher<sup>r</sup> R.Flaminio<sup>c</sup> G.Fluegge<sup>b</sup> N.Fouque<sup>v</sup> Yu.Galaktionov<sup>aa,l</sup> M.Gervasi<sup>v</sup> P.Giusti<sup>l</sup> W.Q.Gu<sup>h</sup> T.G.Guzik<sup>e</sup> K.Hangarter<sup>b</sup> A.Hasan<sup>af</sup> V.Hermel<sup>c</sup> H.Hofer<sup>af</sup> M.A.Huang<sup>ac</sup> W.Hungerford<sup>af</sup> M.Ionica<sup>k</sup> R.Ionica<sup>k</sup> J.Isbert<sup>e</sup> M.Jongmanns<sup>af</sup> W.Karpinski<sup>a</sup> G.Kenney<sup>af</sup> J.Kenny<sup>ab</sup> W.Kim<sup>ad</sup> A.Klementov<sup>l,aa</sup> J.Krieger<sup>l,1</sup> R.Kossakowski<sup>c</sup> V.Koutsenko<sup>l,aa</sup> G.Laborie<sup>s</sup> T.Laitinen<sup>ae</sup> G.Lamanna<sup>ab</sup> G.Laurenti<sup>l</sup> A.Lebedev<sup>l</sup> S.C.Lee<sup>ac</sup> G.Levi<sup>i</sup> P.Levtchenko<sup>ab,2</sup> T.P.Li<sup>l</sup> C.L.Liu<sup>w</sup> H.T.Liu<sup>i</sup> M.Lolli<sup>l</sup> I.Lopes<sup>n</sup> G.Lu<sup>g</sup> Y.S.Lu<sup>i</sup> K.Lübelsmeyer<sup>a</sup> D.Luckey<sup>l</sup> W.Lustermann<sup>af</sup> G.Maehlum<sup>ab,3</sup> C.Maňa<sup>x</sup> A.Margotti<sup>l</sup> F.Massera<sup>l</sup> F.Mayet<sup>s</sup> R.R.McNeil<sup>e</sup> B.Meillon<sup>s</sup> M.Menichelli<sup>ab</sup> F.Mezzanotte<sup>r</sup> R.Mezzenga<sup>ab</sup> A.Mihul<sup>k</sup> G.Molinari<sup>l</sup> A.Mourao<sup>u</sup> A.Mujunen<sup>t</sup> F.Palmonari<sup>l</sup> G.Pancaldi<sup>l</sup> A.Papi<sup>ab</sup> I.H.Park<sup>ad</sup> M.Pauluzzi<sup>ab</sup> F.Pauss<sup>af</sup> E.Perrin<sup>l</sup> A.Pesci<sup>l</sup> A.Pevsner<sup>l</sup> R.Pilastrini<sup>l</sup> M.Pimenta<sup>v,u</sup> V.Plyaskin<sup>aa</sup> V.Pojidaev<sup>aa</sup> H.Postema<sup>l,4</sup> E.Pratil<sup>i</sup> N.Produit<sup>t</sup> P.G.Rancoita<sup>y</sup> D.Rapin<sup>l</sup> F.Raupach<sup>a</sup> S.Recupero<sup>l</sup> D.Ren<sup>af</sup> Z.Ren<sup>ac</sup> M.Ribordy<sup>r</sup> J.P.Richeux<sup>r</sup> E.Riihonen<sup>ae</sup> J.Ritakari<sup>t</sup> U.Roeser<sup>af</sup> C.Roissin<sup>s</sup> R.Sagdeev<sup>v</sup> D.Santos<sup>s</sup> G.Sartorelli<sup>l</sup> A.Schultz von Dratzig<sup>a</sup> G.Schowering<sup>a</sup> V.Shoutko<sup>l</sup> E.Shoumилov<sup>aa</sup> R.Siedling<sup>a</sup> D.Son<sup>ad</sup> T.Song<sup>h</sup> M.Steuer<sup>l</sup> G.S.Sun<sup>h</sup> H.Suter<sup>af</sup> X.W.Tang<sup>l</sup> Samuel C.C.Ting<sup>l</sup> S.M.Ting<sup>l</sup> F.Tenbusch<sup>a</sup> G.Torromeo<sup>l</sup> J.Torsti<sup>ae</sup> J.Trümper<sup>q</sup> J.Ulbricht<sup>af</sup> S.Urpo<sup>l</sup> I.Usovkin<sup>y</sup> E.Valtonen<sup>ae</sup> J.Vandenhirtz<sup>a</sup> E.Velikhov<sup>z</sup> B.Verlaat<sup>af,5</sup> I.Vetlitsky<sup>aa</sup> F.Vezzu<sup>s</sup> J.P.Vialle<sup>c</sup> G.Viertel<sup>af</sup> D.Vité<sup>l</sup> H.Von Gunten<sup>af</sup> S.Waldmeier Wicki<sup>af</sup> W.Wallraff<sup>a</sup> B.C.Wang<sup>w</sup> J.Z.Wang<sup>g</sup> Y.H.Wang<sup>ac</sup> J.P.Wefel<sup>e</sup> E.A.Werner<sup>a,1</sup> C.Williams<sup>t</sup> S.X.Wu<sup>l,4</sup> P.C.Xia<sup>h</sup> J.L.Yan<sup>g</sup> L.G.Yan<sup>h</sup> C.G.Yang<sup>i</sup> M.Yang<sup>i</sup> P.Yeh<sup>ac</sup> H.Y.Zhang<sup>f</sup> D.X.Zhao<sup>h</sup> G.Y.Zhu<sup>i</sup> W.Z.Zhu<sup>g</sup> H.L.Zhuang<sup>l</sup> A.Zichichi<sup>j</sup>

<sup>a</sup> I. Physikalisches Institut, RWTH, D-52056 Aachen, Germany<sup>6</sup>

<sup>b</sup> III. Physikalisches Institut, RWTH, D-52056 Aachen, Germany<sup>6</sup>

<sup>c</sup> Laboratoire d'Annecy-le-Vieux de Physique des Particules, LAPP, F-74941 Annecy-le-Vieux CEDEX, France

<sup>d</sup> Louisiana State University, Baton Rouge, LA 70803, USA

<sup>e</sup> Johns Hopkins University, Baltimore, MD 21218, USA

<sup>f</sup> Center of Space Science and Application, Chinese Academy of Sciences, 100080 Beijing, China

<sup>g</sup> Chinese Academy of Launching Vehicle Technology, CALT, 100076 Beijing, China

<sup>h</sup> Institute of Electrical Engineering, IEE, Chinese Academy of Sciences, 100080 Beijing, China

<sup>i</sup> Institute of High Energy Physics, IHEP, Chinese Academy of Sciences, 100039 Beijing, China<sup>7</sup>

<sup>j</sup> University of Bologna and INFN-Sezione di Bologna, I-40126 Bologna, Italy

<sup>k</sup> Institute of Microtechnology, Politechnica University of Bucharest and University of Bucharest, R-76900 Bucharest, Romania

<sup>l</sup> Massachusetts Institute of Technology, Cambridge, MA 02139, USA

<sup>m</sup> National Central University, Chung-Li, Taiwan 32054

<sup>n</sup> Laboratorio de Instrumentacao e Fisica Experimental de Particulas, LIP, P-3000 Coimbra, Portugal

<sup>o</sup> University of Maryland, College Park, MD 20742, USA

<sup>p</sup> INFN Sezione di Firenze, I-50125 Florence, Italy

<sup>q</sup> Max-Plank Institut fur Extraterrestrische Physik, D-85740 Garching, Germany

<sup>r</sup> University of Geneva, CH-1211 Geneva 4, Switzerland

<sup>s</sup> Institut des Sciences Nucléaires, F-38026 Grenoble, France

<sup>t</sup> Helsinki University of Technology, FIN-02540 Kylmala, Finland

<sup>u</sup> Instituto Superior Técnico, IST, P-1096 Lisboa, Portugal

<sup>v</sup> Laboratorio de Instrumentacao e Fisica Experimental de Particulas, LIP, P-1000 Lisboa, Portugal

<sup>w</sup> Chung-Shan Institute of Science and Technology, Lung-Tan, Tao Yuan 325, Taiwan 11529

<sup>x</sup> Centro de Investigaciones Energéticas, Medioambientales y Tecnológicas, CIEMAT, E-28040 Madrid, Spain<sup>8</sup>

<sup>y</sup> INFN-Sezione di Milano, I-20133 Milan, Italy

<sup>z</sup> Kurchatov Institute, Moscow, 123182 Russia

<sup>aa</sup> Institute of Theoretical and Experimental Physics, ITEP, Moscow, 117259 Russia

<sup>ab</sup> INFN-Sezione di Perugia and Università Degli Studi di Perugia, I-06100 Perugia, Italy<sup>9</sup>

<sup>ac</sup> Academia Sinica, Taipei, Taiwan

<sup>ad</sup> Kyungpook National University, 702-701 Taegu, Korea

<sup>ae</sup> University of Turku, FIN-20014 Turku, Finland

<sup>af</sup> Eidgenössische Technische Hochschule, ETH Zürich, CH-8093 Zürich, Switzerland

<sup>1</sup> Now at ISATEC, Aachen, Germany.

<sup>2</sup> Permanent address: Nuclear Physics Institute, St. Petersburg, Russia.

<sup>3</sup> Now at IDE-AS, Oslo, Norway.

<sup>4</sup> Now at European Laboratory for Particle Physics, CERN, CH-1211 Geneva 23, Switzerland.

<sup>5</sup> Now at National Institute for High Energy Physics, NIKHEF, NL-1009 DB Amsterdam, The Netherlands.

<sup>6</sup> Supported by the Deutsches Zentrum für Luft- und Raumfahrt, DLR.

<sup>7</sup> Supported by the National Natural Science Foundation of China.

<sup>8</sup> Supported also by the Comisión Interministerial de Ciencia y Tecnología.

<sup>9</sup> Also supported by the Italian Space Agency.

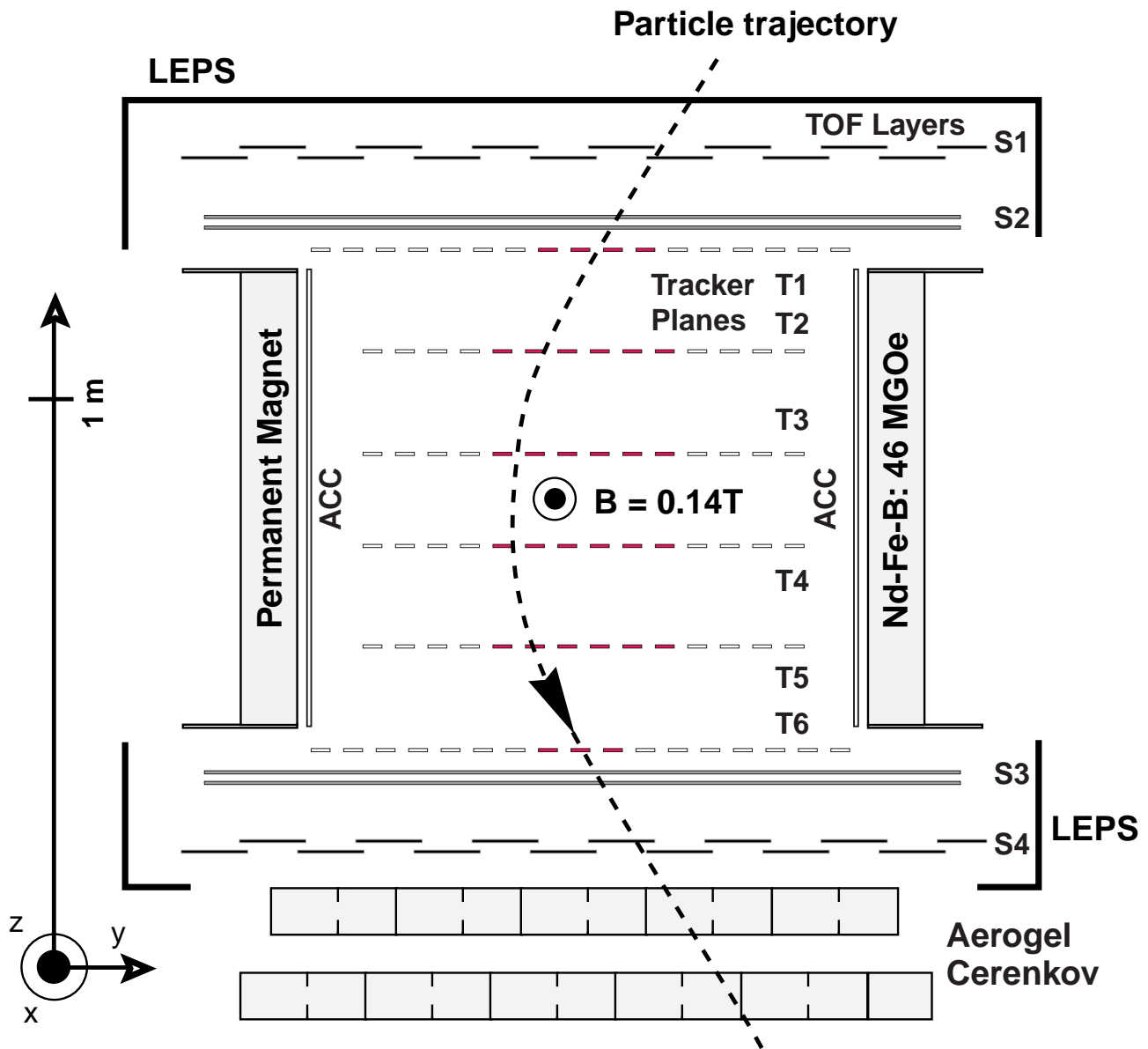


Figure 1: Schematic view of AMS as flown on STS-91 showing the cylindrical permanent magnet, the silicon microstrip tracker planes T1 to T6, the time of flight (TOF) hodoscope layers S1 to S4, the aerogel cerenkov counter, the anticoincidence counters (ACC) and low energy particle shields (LEPS).

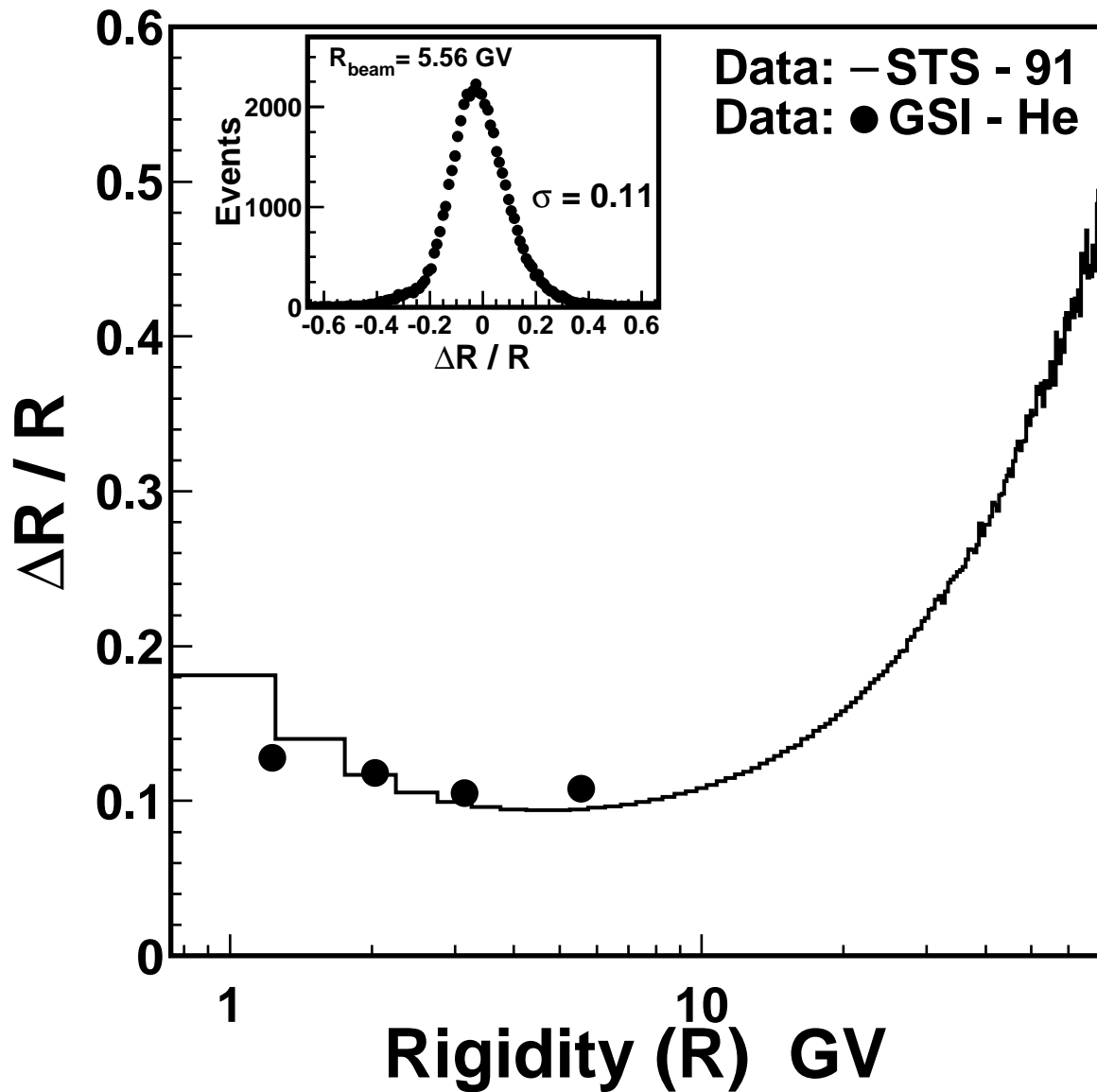


Figure 2: Rigidity resolution for  $|Z| = 2$  flight data (histogram) compared with the GSI He test beam (points).

Inset: Typical rigidity resolution,  $\Delta R / R = (R_{measured} - R_{beam}) / R_{beam}$ , from the GSI He data.

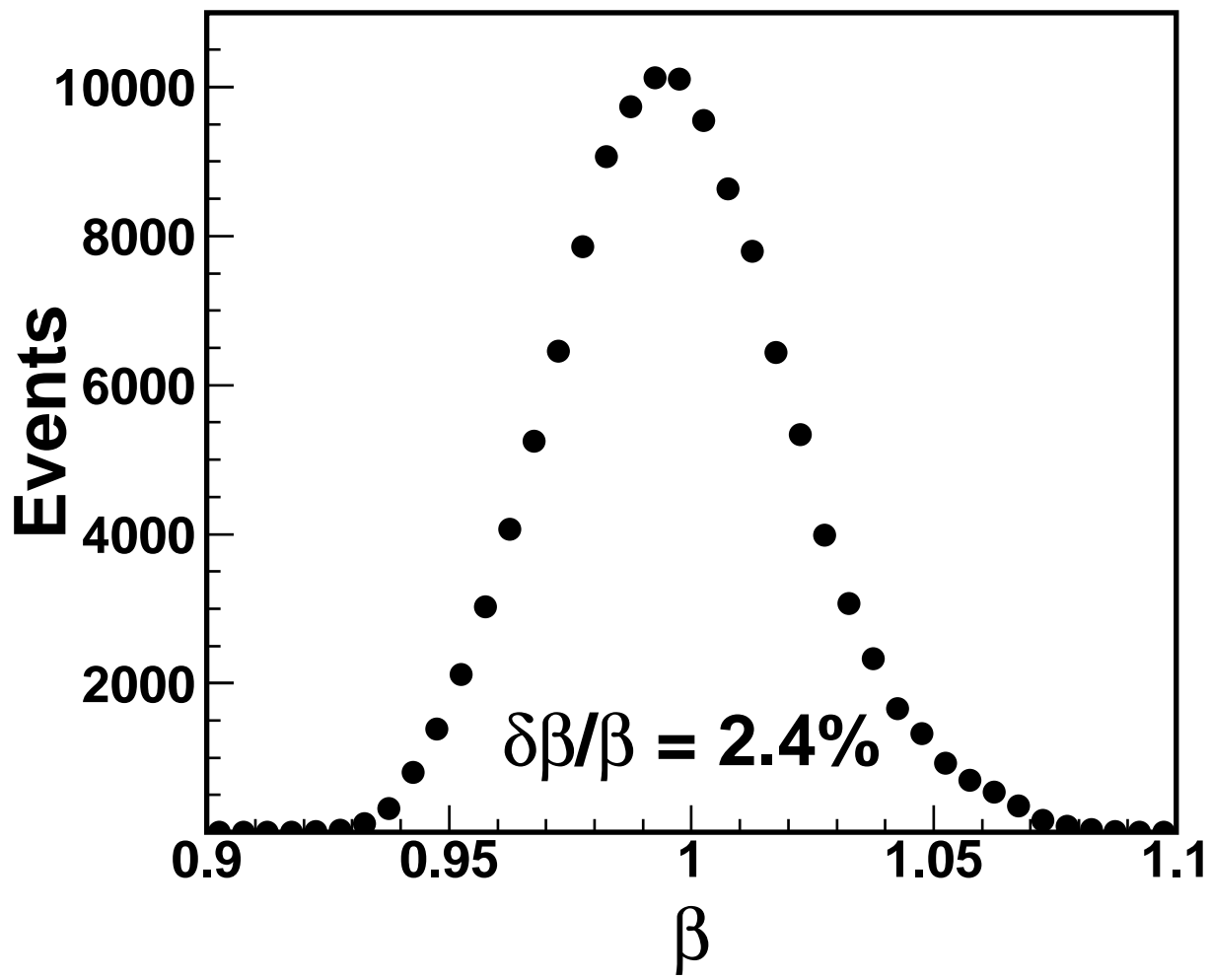


Figure 3: Measured velocity,  $\beta = v/c$ , distribution for  $|Z| = 2$  events with  $R > 16$  GV.

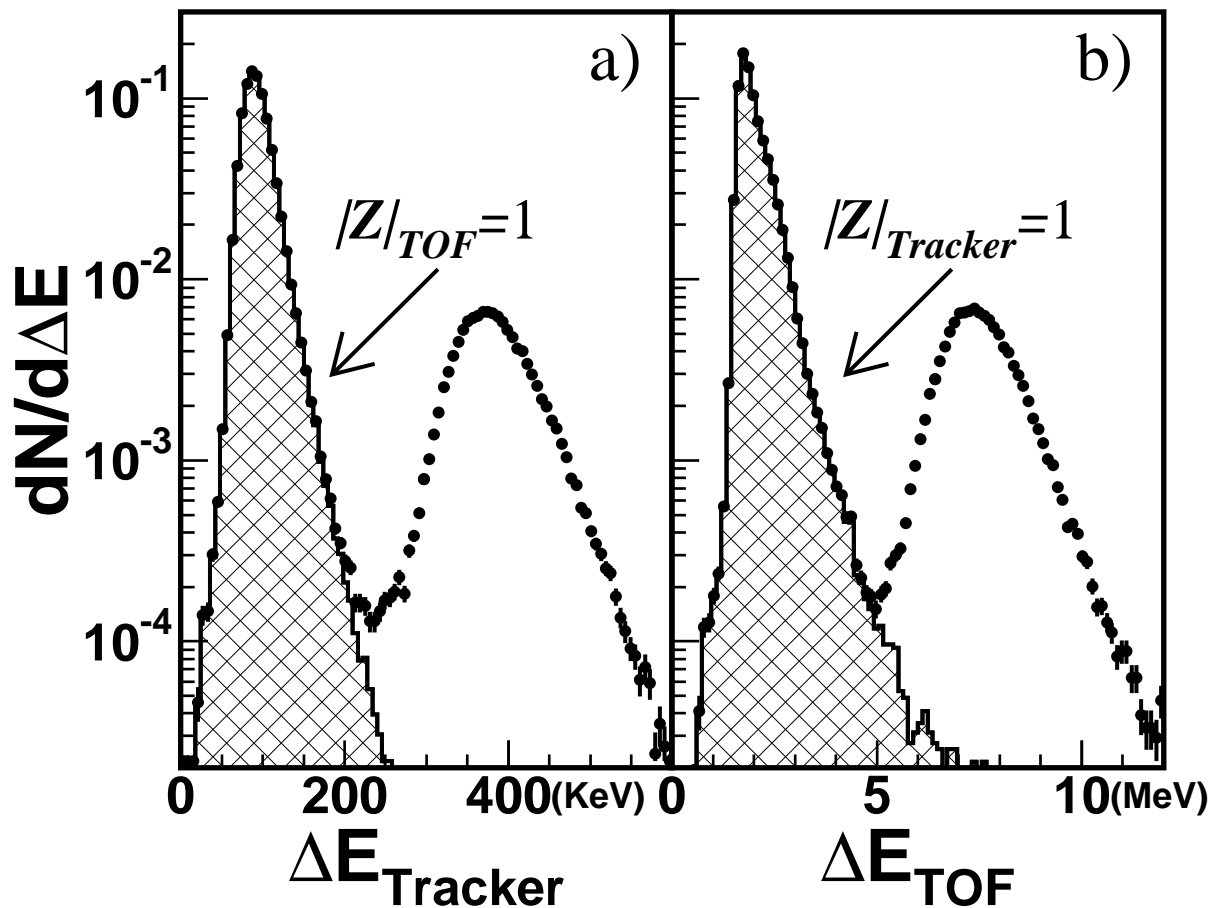


Figure 4: Energy loss measurements (points) are made independently in the tracker (a) and TOF (b) for  $|Z| \leq 2$  events. The hatched histogram shows which events were assigned to be  $|Z| = 1$  by the other detector.

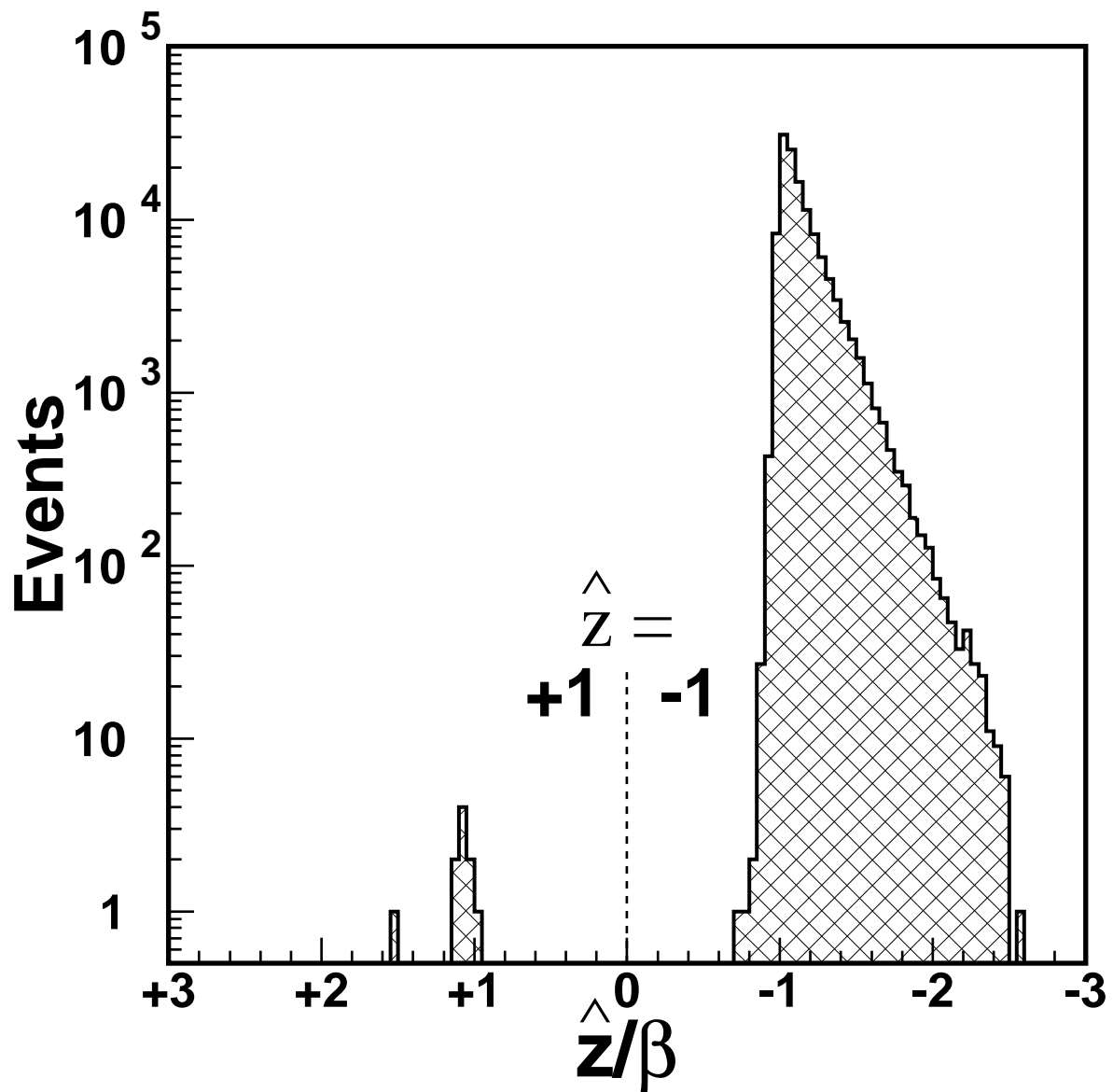


Figure 5: A typical direction,  $\hat{z}/\beta$ , distribution for  $|Z| = 2$  events. As seen, the  $\hat{z} = +1$  (or upward) and  $\hat{z} = -1$  (or downward) populations are clearly separated.

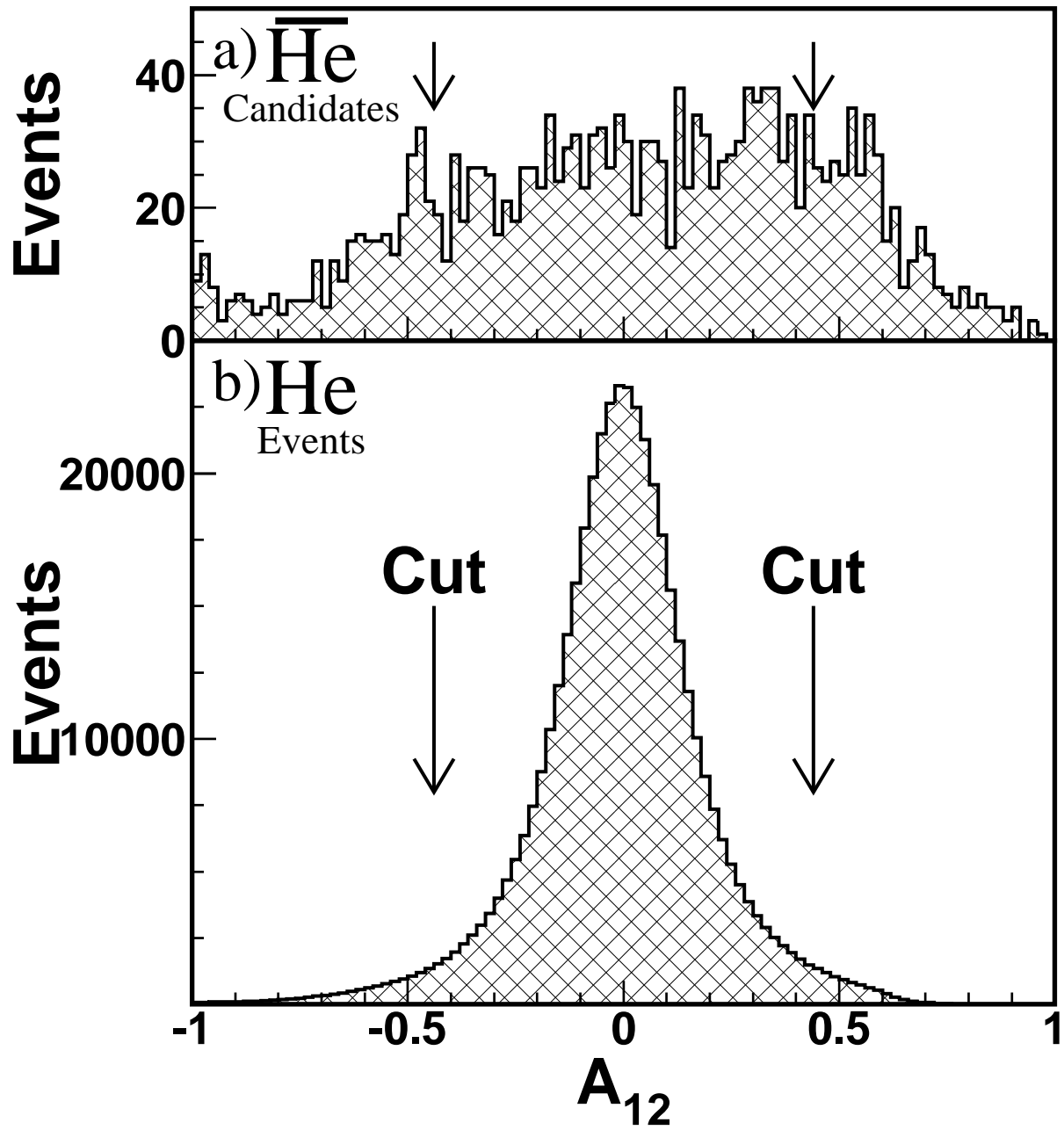


Figure 6: The asymmetry,  $A_{12} = (R_1 - R_2)/(R_1 + R_2)$ , of the rigidity measurements using the first,  $R_1$ , and last,  $R_2$ , three hits along the track for  $|Z| = 2$  events. Also shown are the cuts used. As seen the  $A_{12}$  cuts reject much of the large angle scattering events (a). The cuts do not reject the genuine signal (b).

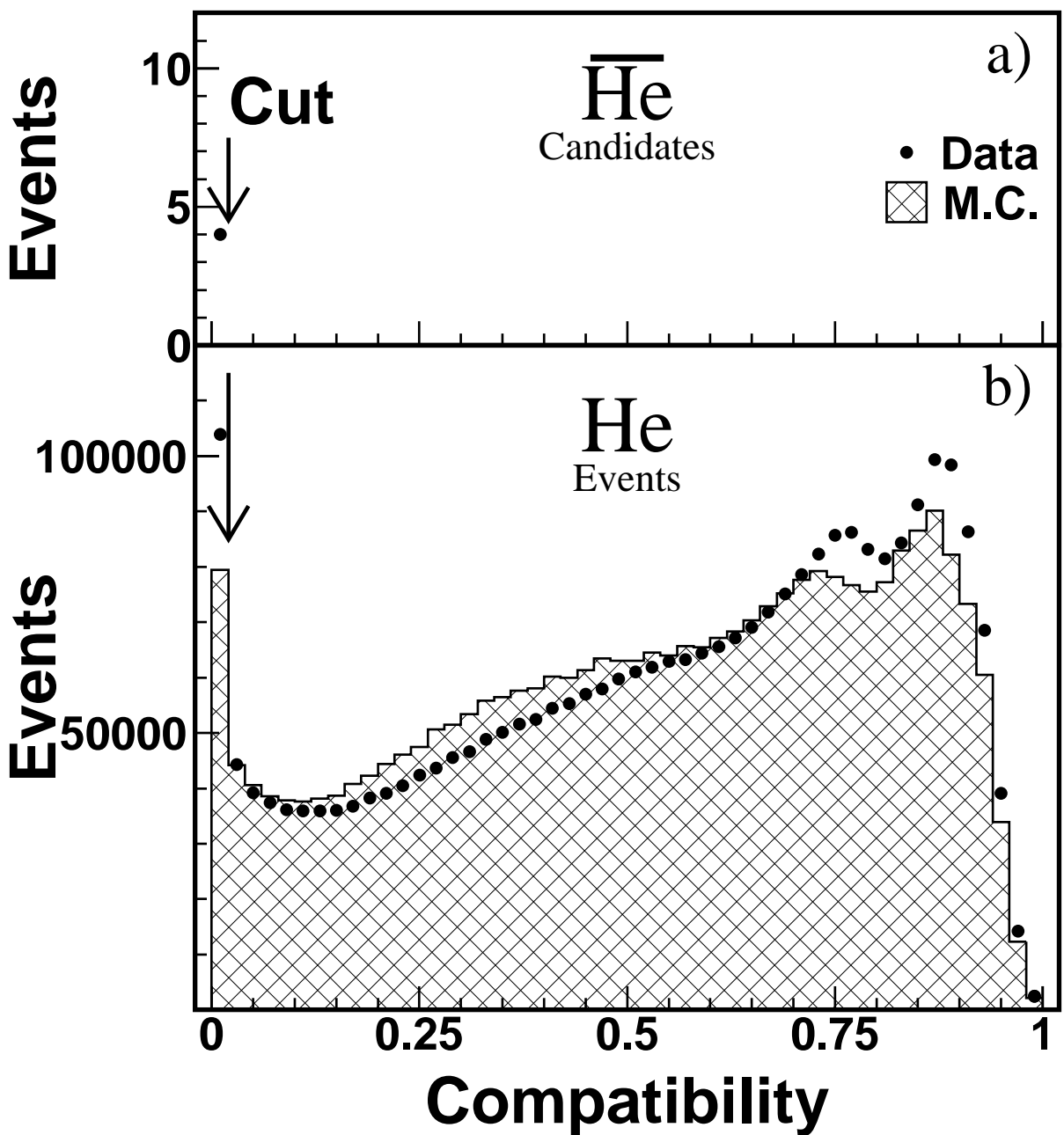


Figure 7: (a) Compatibility of the measured event parameters,  $\beta$ , R and  $|Z|$ , to be an  $\overline{\text{He}}$  nucleus.  
(b) Compatibility to be a He nucleus. The hatched histogram is the Monte Carlo prediction for He nuclei.

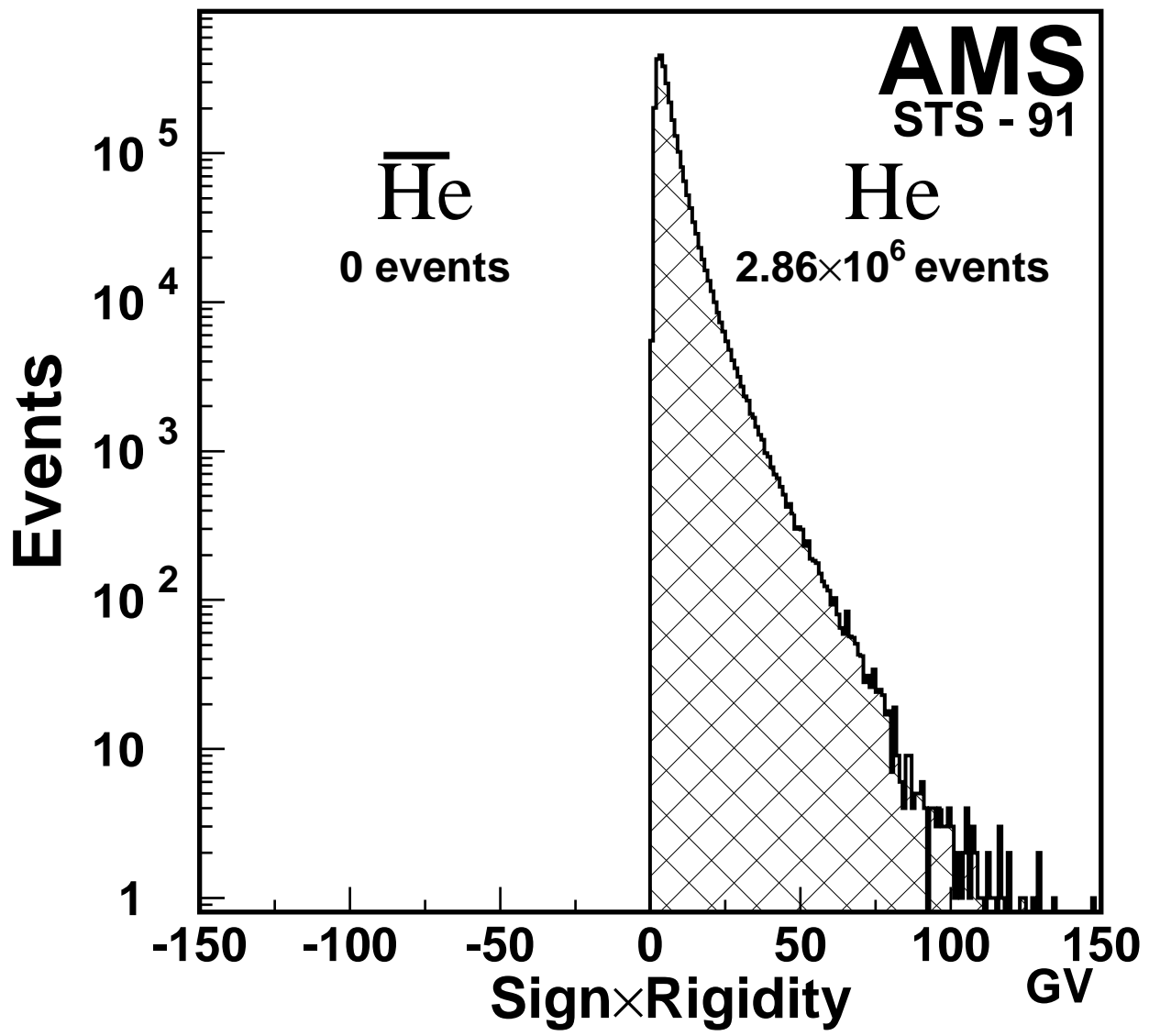


Figure 8: Measured rigidity times the charge sign for selected  $|Z| = 2$  events.

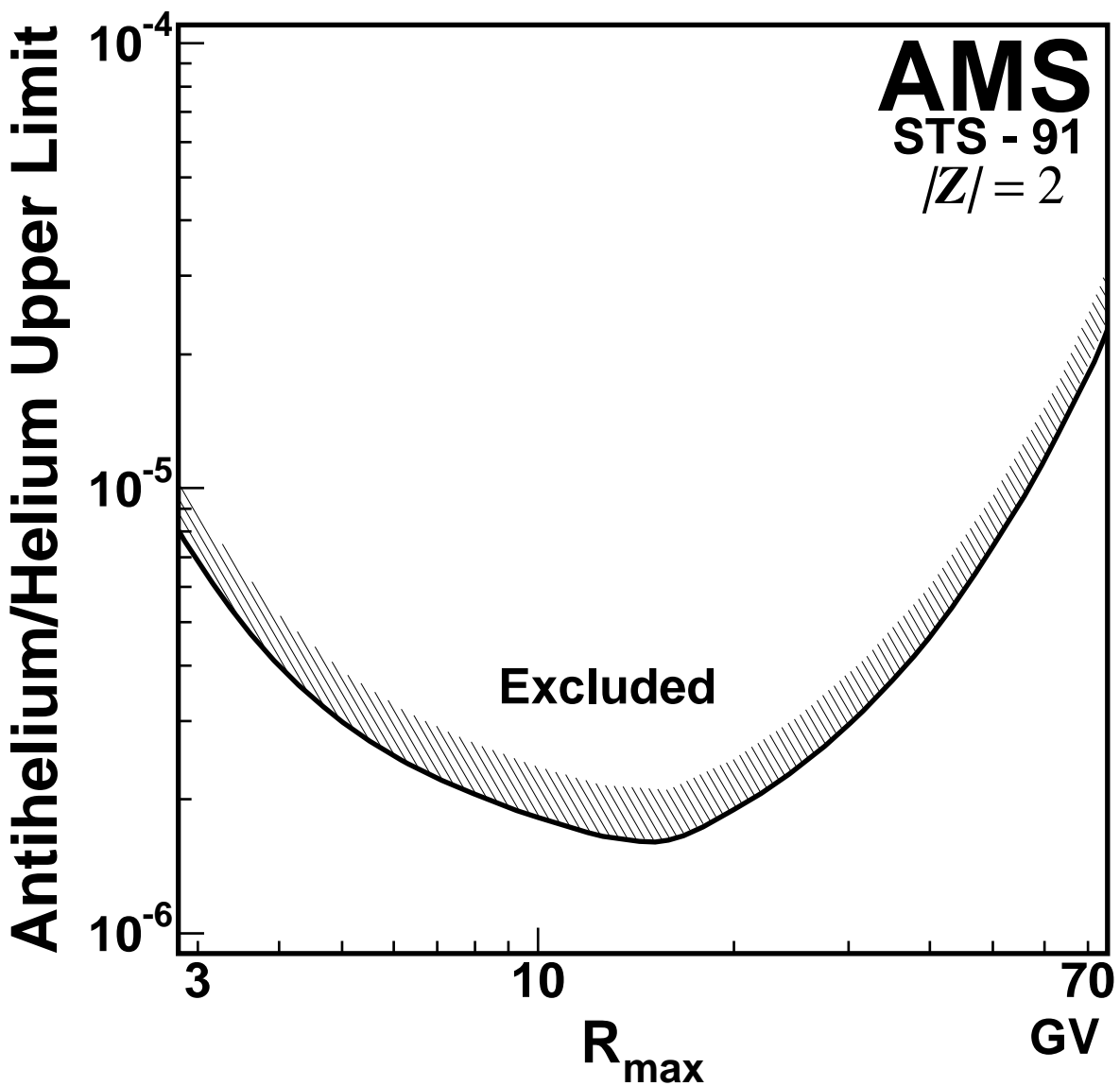


Figure 9: Upper limits on the relative flux of antihelium to helium, at the 95% confidence level, as a function of the rigidity interval  $R = 1.6 \text{ GV}$  to  $R_{max}$ . These results are independent of the incident antihelium spectra.